Côte d'Ivoire–Ghana margin: seismic imaging of passive rifted crust adjacent to a transform continental margin

C. Peirce,[1] R. B. Whitmarsh,[2,*] R. A. Scrutton,[3] B. Pontoise,[4] F. Sage[4] and J. Mascle[5]

[1] *Department of Geological Sciences, University of Durham, Science Laboratories, South Road, Durham, DH1 3LE, UK*

[2] *Institute of Oceanographic Sciences, Deacon Laboratory, Brook Road, Wormley, Godalming, Surrey, GU8 5UB, UK*

[3] *Department of Geology and Geophysics, Grant Institute, West Mains Road, Edinburgh, EH9 3JW, UK*

[4] *ORSTOM—Laboratoire de Géodynamique sous Marine, BP 48, 06230 Villefranche sur mer, France*

[5] *GEMCO—Laboratoire de Géodynamique sous Marine, BP 48, 06230 Villefranche sur mer, France*

SUMMARY

During May 1990 and January–February 1991, an extensive geophysical data set was collected over the Côte d'Ivoire–Ghana continental margin, located along the equatorial coast of West Africa. The Ghana margin is a transform continental margin running subparallel to the Romanche Fracture Zone and its associated marginal ridge—the Côte d'Ivoire–Ghana Ridge. From this data set, an explosive refraction line running ~150 km, ENE–WSW between 3°55'N, 3°21'W and 4°23'N, 2°4'W, has been modelled together with wide-angle airgun profiles, and seismic reflection and gravity data. This study is centred on the Côte d'Ivoire Basin located just to the north of the Côte d'Ivoire–Ghana Ridge, where bathymetric data suggest that a component of normal rifting occurred, rather than the transform motion observed along the majority of the equatorial West African margin.

Traveltime and amplitude modelling of the ocean-bottom seismometer data shows that the continental Moho beneath the margin rises in an oceanward direction, from ~24 km below sea level to ~17 km. In the centre of the line where the crust thins most rapidly, there exists a region of anomalously high velocity at the base of the crust, reaching some 8 km in thickness. This higher-velocity region is thought to represent an area of localized underplating related to rifting. Modelling of marine gravity data, collected coincident with the seismic line, has been used to test the best-fitting seismic model. This modelling has shown that the observed free-air anomaly is dominated by the effects of crustal thickness, and that a region of higher density is required at the base of the crust to fit the observed data. This higher-density region is consistent in size and location with the high velocities required to fit the seismic data.

Key words: continental margin, Côte d'Ivoire–Ghana, OBS, seismic structure.

1 INTRODUCTION

Transform margins were first recognized by Wilson (1965) in terms of their relationship to offsets in mid-ocean ridge geometries. Wilson (1965) observed that these margins appear to be connected to ridge offsets by the traces of inactive fracture zones, whose only active part is located between the ends of the offset spreading segments. Transform margins are thought to be formed by the rifting of continental crust along the fracture zone, adjacent to which the crust may be increasingly thinned and rifted as the continents progressively move apart until eventually, newly formed oceanic crust is juxtaposed against the continental margin on the opposite side of the transform fault (Mascle & Blarez 1987). As the newly created spreading centre passes the margin laterally, it causes heating and thermal uplift of points along the adjacent continent. Once the spreading centre has passed by, shearing ceases and the margin thermally subsides (Le Pichon & Hayes 1971; Mascle & Blarez 1987; Mascle et al. 1996; Edwards, Whitmarsh & Scrutton 1996).

A number of geophysical experiments have been conducted across transform margins to determine crustal structure and mode of formation in different tectonic settings. Dehlinger

* Now at: Southampton Oceanography Centre, Empress Dock, European Way, Southampton, SO14 3ZH, UK.

et al. (1970) developed structural cross-sections across the Queen Charlotte Islands Fault based upon gravity and seismic refraction surveys. Recq (1982) proposed a model for the Davie Fracture Zone based on traveltime residuals. However, only Todd, Reid & Keen (1988) and Lorenzo et al. (1991) have modelled profiles shot specifically across transform margins, at the Newfoundland Fracture Zone and Exmouth Plateau respectively. Todd et al. (1988) observed that the continental crust beneath the Newfoundland margin thins oceanwards from ~30 km thick beneath the Southern Grand Banks, to a 20 km wide transition zone containing oceanic volcanics and syn-rift sediments. Seawards of the transition zone, the crust is oceanic in character with a velocity gradient from 4.7 to 6.5 km s^{-1} and a thickness of 7–8 km, but anomalous in that oceanic layer 3 is absent. Also, beneath the Newfoundland margin there is no significant thickness of high-velocity material (7.0–7.4 km s^{-1}) at the continent–ocean transition, indicating that no underplating of the continental crust has occurred. On the other hand, beneath the Exmouth Plateau (Lorenzo et al. 1991) the continental crust thins in an oceanward direction from about 22 km thick beneath the shelf region to 7–8 km thick beneath the deep ocean, where it exhibits velocities similar to those of oceanic layer 3. The most unusual feature of this profile, however, is a 10 km thick layer of velocity 7.2–7.4 km s^{-1} at the base of the crust beneath the continental shelf/break of slope. Deep crustal layers with velocities in this range have been attributed to magmatic underplating of extended continental crust (e.g. White et al. 1987; LASE Study Group 1986), as a result of decompression melting of thinned lithosphere (White & McKenzie 1989). Therefore, no one simple model currently appears to satisfy the observations to date. Hence, a major study was undertaken

to determine the detailed structure of a transform margin in an environment tectonically different from those previously described and to formulate a general model for transform-margin evolution of which the data presented here forms one part of the jigsaw.

The area chosen for study is the east–west-trending, equatorial coast of West Africa (offshore Ghana and the Côte d'Ivoire), which, in contrast to the Newfoundland margin, represents a ruptured craton rather than a ruptured orogenic belt. The Ghana margin, formed by the break-up of Africa and South America, was selected because it had already been extensively surveyed using seismic reflection, gravity, magnetic and bathymetric methods (e.g. Fail et al. 1970; Sibuet & Mascle 1978; Delteil et al. 1974; Mascle & Blarez 1987; Basile, Brun & Mascle 1992; Basile et al. 1993), and hence the upper-crustal structure was already relatively well constrained. The Ghana transform margin is approximately 550 km in length, and is characterized by a rather linear geometry, controlled by the Romanche Fracture Zone, and runs roughly parallel with the equator.

Sea-floor spreading began off Ghana during Aptian–Albian times (~110 Ma—Mascle & Blarez 1987). Subsequent spreading and differential motion across the Romanche Fracture Zone to the present day are thought to have juxtaposed normal continental crust against oceanic crust along this margin offshore Ghana (Mascle & Blarez 1987). The geometry of the margin offshore the Côte d'Ivoire, as shown by bathymetry data, also tends to suggest that some component of normal rifting has taken place in localized areas, and hence this location provides an ideal target for investigating a wide variety of pure-transform to pure-rifted margin types. The purpose of the seismic refraction survey presented here is to
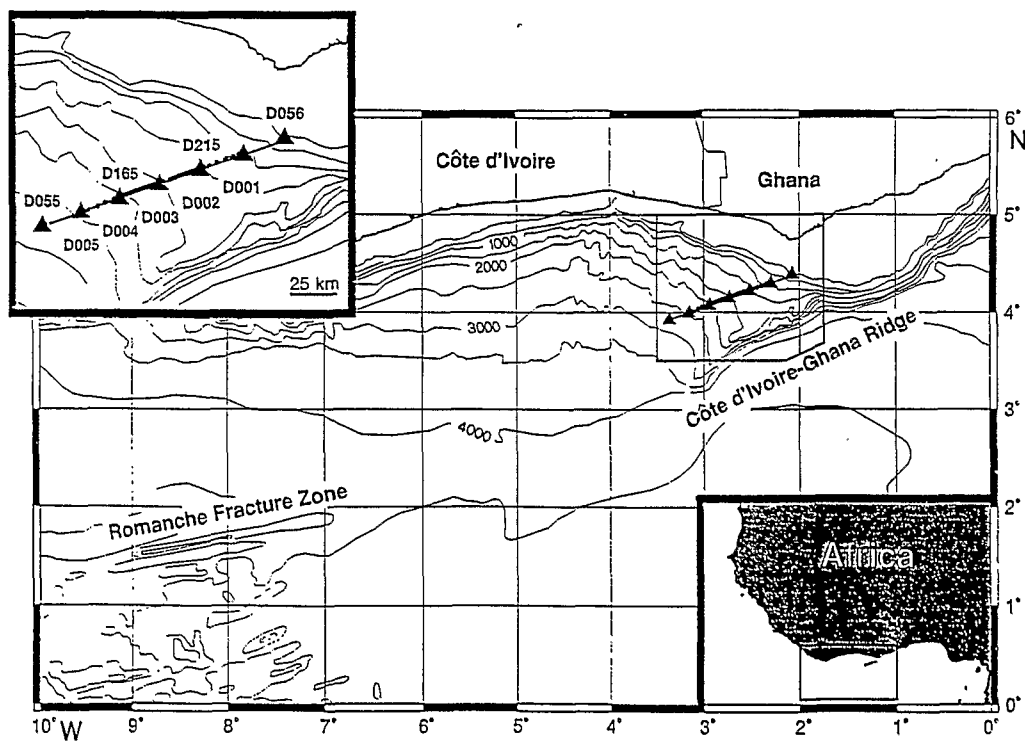

Figure 1. Location of the Côte d'Ivoire–Ghana continental margin. Triangles show instrument locations and dots explosive shots. Contours are in metres. The solid line represents the location of the airgun profile. Inserts show the regional location of the margin and the details of the seismic experiment.

define the crustal velocity structure beneath the apparently rifted part of the margin north of the Côte d'Ivoire–Ghana marginal ridge and complement the information provided by seismic reflection and gravity studies (Fig. 1).

2 THE EXPERIMENT

An extensive geophysical data set was collected offshore the Côte d'Ivoire and Ghana during three research cruises: two in 1990 aboard the NO Nadir (cruise EQUASIS—multichannel seismic reflection data collection; cruise EQUAREF—seismic refraction data collection principally over the margin adjacent to the Côte d'Ivoire–Ghana Ridge), and the other in 1991 aboard the RRS Charles Darwin (cruise CD55) located principally over the Ghana transform margin, with survey lines either side and across the postulated extension of the Romanche Fracture Zone. The principal objectives of these cruises were (see Fig. 1):

(1) to study the deep crustal structure across the continent–ocean transition off Ghana where the equatorial Romanche Fracture Zone strongly influences the shape of the continental slope and truncates normal (unrifted) continental crust;

(2) to study the crustal structure of the Côte d'Ivoire–Ghana Ridge and the adjacent deep Côte d'Ivoire Basin; and

(3) to investigate the location of the continent–ocean transition and determine how this boundary changes with offset along the transform margin.

The total data set includes numerous multichannel seismic reflection lines (Sage 1994), underway gravity, magnetic and bathymetric data, plus 17 wide-angle seismic refraction lines recorded by ocean-bottom seismometers (OBSs). In this paper we aim to present the results of traveltime and amplitude modelling of a reversed profile collected in the Côte d'Ivoire Basin at the western end of the Ghana margin, where bathymetric data suggest that orthogonal rifting may have taken place (see Fig. 1). The wide-angle refraction data were recorded with nine OBSs from the Institute of Oceanographic Sciences Deacon Laboratory (IOSDL) and the Laboratoire de Géodynamique sous Marine, Villefranche sur mer. Details of the experimental configuration are shown in Fig. 1. The data set was collected in two stages. First, a wide-angle seismic line running approximately 150 km, ENE–WSW between 3°55′N, 3° 21′W and 4°23′N, 2°4′W, and traversing the roughly NW–SE-trending continental slope (see Fig. 1), was shot during cruise EQUAREF with seven equally spaced OBSs. Unfortunately, a number of instruments located in the centre of the EQUAREF line suffered technical problems during shooting, and therefore the line was re-shot during CD55 using two OBSs to re-occupy two of the mid-line sites and two others to extend the ends of the line, with the aim of completing and fully reversing the existing profiles. The EQUAREF OBSs recorded shots fired at 90 s intervals, using an untuned, 8000 cu.in. ($\sim$131.2 l) airgun array. Two of these OBSs were deployed with a vertical-component geophone and a hydrophone as sensors. The remaining instruments were deployed with a three-component geophone package only. The EQUAREF line was surveyed at a speed of 4 knots ($\sim$7.5 km hr^{-1}), generating a shot spacing of approximately 180 m. The CD55 OBSs were located approximately 50 km apart and recorded 38 explosive shots, ranging in size from 25

to 125 kg, using a three-component geophone package and a hydrophone as sensors. At a surveying speed of approximately 10 knots ($\sim$19.0 km hr^{-1}) and a shot-firing interval of 6 min, this provided an average shot spacing of about 2 km. Shot–receiver ranges were calculated using a technique based on matching observed water-wave arrival times by ray tracing through the water column, whose velocity structure was measured while at sea. Instrument ranges were then adjusted slightly until recorded water-wave traveltimes matched calculated hodochrons for each instrument location. The close shot spacing of the airgun data provides detailed information not only on the upper-crustal velocity structure (both vertical and horizontal variations in velocity gradient) adjacent to each instrument, but also on the variation in signal amplitude with offset. The lower-frequency explosive data provide information on the deeper crustal structure.

As part of the EQUASIS cruise, 24-fold normal-incidence seismic reflection data were collected coincident with the wide-angle line. The normal-incidence data show the main near-surface features in some detail and were used mainly to provide control on the sediment structure and depth to basement for the wide-angle ray-trace model (see Section 4).

3 MODELLING METHOD AND RESULTS

The OBS data were traveltime and amplitude modelled using a ray-trace technique based on the Maslov asymptotic ray theory of Chapman & Drummond (1982). Initially, the data from each OBS were interpreted using a simple 1-D slope-intercept traveltime inversion method, to give an estimate of the velocity–depth structure adjacent to each instrument. These velocity–depth profiles were combined to form the initial 2-D model. The sedimentary structure and depth to acoustic basement were initially obtained from the 1-D interpretations and later verified with the normal-incidence reflection profile when it became available (see Section 4). To simplify the initial modelling, the sedimentary sequence was represented by a single layer, with initial *P*-wave velocity estimates obtained from compilations of laboratory rock densities and velocities (e.g. Nafe & Drake 1957, 1962; Ludwig, Nafe & Drake 1970; Hamilton 1978). The seabed interface along the entire length of the model was constructed from underway bathymetric measurements made while shooting.

The best-fitting velocity–depth model was obtained using the trial-and-error method outlined in Peirce (1990) and Peirce & Barton (1991), where a model is ray traced, the fit of synthetic traveltimes and amplitudes to the observations assessed, the model adjusted accordingly and re-traced. When a reasonable fit is obtained for one particular instrument, the model is tested with all remaining OBS data (see Peirce and Peirce & Barton *op. cit.* for assessment criteria). The modelling procedure was conducted as follows.

(1) The traveltimes of direct water waves and multiple events were modelled as a check on each instrument's relative location and deployed water depth. This step also provided a check on the shot–receiver range calculations conducted to produce the observed wide-angle seismic sections.

(2) Once a consistent set of receiver–receiver and shot–receiver ranges and receiver depths was obtained, upper-crustal, close-offset arrivals (*Ps* and *Pg* phases) were modelled, in the first instance to constrain the sediment thickness and

velocity structure and also to constrain the geometry of the sediment–acoustic basement interface. The velocity structure obtained at each instrument was interpolated along the model to provide a smooth transition between instrument locations.

(3) Once a consistent near-surface structure had been obtained from the above two steps, lower-crust and upper-mantle arrivals (*Pg* and *Pn* phases) were modelled by adjusting the crustal velocity structure and interface geometry while leaving the upper-crustal structure unchanged. At this stage, intracrustal interfaces (first-order discontinuities) or changes in velocity gradient (second-order discontinuities) could be incorporated as necessary.

(4) Finally, Moho reflections (*PmP* phases) were used to constrain the exact geometry of, and the velocity contrast across, the crust–mantle boundary.

(5) Once a consistent 'best-fitting' model had been achieved for one particular OBS profile, all other profiles were modelled to check for not only a good traveltime fit, but also a match of amplitude variations as a function of offset. If necessary, velocity gradients (horizontal and vertical) and contrasts across interfaces were adjusted and rechecked for all instruments until a good overall fit, consistent with all OBSs, was obtained.

During ray tracing, we concentrated mainly on modelling the first arrivals of energy at each OBS, particularly the sediment and crustal phases, Moho reflections and the variation in amplitude across the crust–mantle transition. On a number of sections, especially the airgun profiles, a wide variety of later arriving, secondary phases are observed. These arrivals are interpreted as interlayer reflections, *P*- to *S*-wave mode conversions and multiples. We have not attempted to show the fit of these phases on the ray-trace diagrams, for reasons of clarity, although they were modelled to the same degree of fit as the first arrivals. Care was also taken to ensure that good ray coverage was obtained across the entire model for each OBS, thus ensuring accurate calculation of the variation in phase amplitude as a function of offset.

The results of modelling are discussed below, together with a description of the main features of the record sections and the model. Four typical examples of the ray-tracing and synthetic seismograms are shown in Figs 2(a)–(d), together with the corresponding data for comparison. The data and synthetics are plotted at the same scale, oriented with west to the left and plotted with a reduction velocity of 6 km s^{-1}. For the multicomponent instruments, vertical geophone sections are shown in preference to hydrophone records—the latter generally show the same features, but tend to be a little noisier and of a slightly higher frequency content. For modelling purposes, the observed data have been band-pass filtered between 2.0 and 25.0 Hz (explosives) and 5.0 and 14.0 Hz (airguns) and charge-weight balanced (explosives). The filter pass bands were chosen after frequency analysis of the observed data. At frequencies above and below the pass-band limits, both seismic sources provided little energy. The observed and synthetic sections have also had the same linear range scale factor applied to enhance small-amplitude signals at long-range offsets. Both airgun and explosive data quality is good, with, in the case of the airgun data, phases observed at shot offsets of ~70 km from receivers. First and later arrivals are easily identified, and, due to good trace-to-trace coherence, amplitude variations with offset are easily observed. The model presented here generally reproduces traveltimes to within

50–75 ms of the observed, although in the worst case to around 150 ms—the dot size in Figs 2(a)–(d) giving some indication of the misfit. Estimates of the accuracy of the final model were made by adjusting layer velocities, thicknesses and geometries to investigate the effect on the 'goodness of fit' of the synthetic seismograms to the observed data. This exercise was conducted for both traveltimes and amplitudes, and showed that any variation in velocity of more than ±0.10 km s^{-1} or variation in boundary locations of ±0.10 km (upper crust) or ±0.25 km (lower crust) generated an unacceptable fit of the synthetics to the observed data.

3.1 Explosive data

Figs 2(a) and (b) show plots of vertical geophone data recorded by IOSDL' OBSs 165 and 215, and shot with explosives during CD55 (see Fig. 1 for location). The ray-tracing technique allows the incorporation of the seabed geometry and water depth into the model, and hence there proved no need to apply water-column static corrections. Explosive shots, however, have highly variable detonation depths, and hence a small static correction was applied to each traveltime pick to align it with a common datum—i.e. the average shot detonation depth. Shot detonation depths were calculated using a technique based on ray tracing water waves travelling directly from the shot through the water column to the ship, with arrival times measured using a towed hydrophone and a hull-mounted geophone.

The data generally exhibit good signal-to-noise ratios on all channels (X, Y and Z geophone and hydrophone), except at larger offsets (>70 km) where the signal-to-noise ratio approaches unity. Both instruments lie in water depths of greater than 1400 m, and hence the onset of the first sea-surface/seabed multiple does not obscure primary or secondary arrivals. Particular features of these sections are as follows.

(1) First arrivals, mainly crustal diving rays (*Pg*), show significant amplitude variations with range, particularly arrivals that have travelled through the lower crust in the central part of the line, indicating and constraining both horizontal and vertical gradients within the crust.

(2) Significant amplitude loss occurs at ~70 km offset, which is interpreted as the onset of upper-mantle diving rays. The onset and amplitude of these arrivals constrain the crustal thickness and velocity gradient within the upper mantle.

(3) Moho reflections (*PmP* phases) are also observed as secondary arrivals on each section. The exact onset of these phases is uncertain, as they generally arrive close behind the first arrivals and often interfere with the relatively long first-arrival wavelet.

(4) The horizontal-component geophone data contain *P–S* mode-converted phases; no other significant *S*-wave energy is observed.

3.2 Airgun data

Figs 2(c) and (d) show plots of hydrophone data recorded by ORSTOM' OBSs 3 and 5 (see Fig. 1 for locations), and shot using an untuned airgun array as a seismic source. No static corrections were applied to these traveltime picks, as the source array was towed at a constant (within measurement and modelling error) depth through the water.
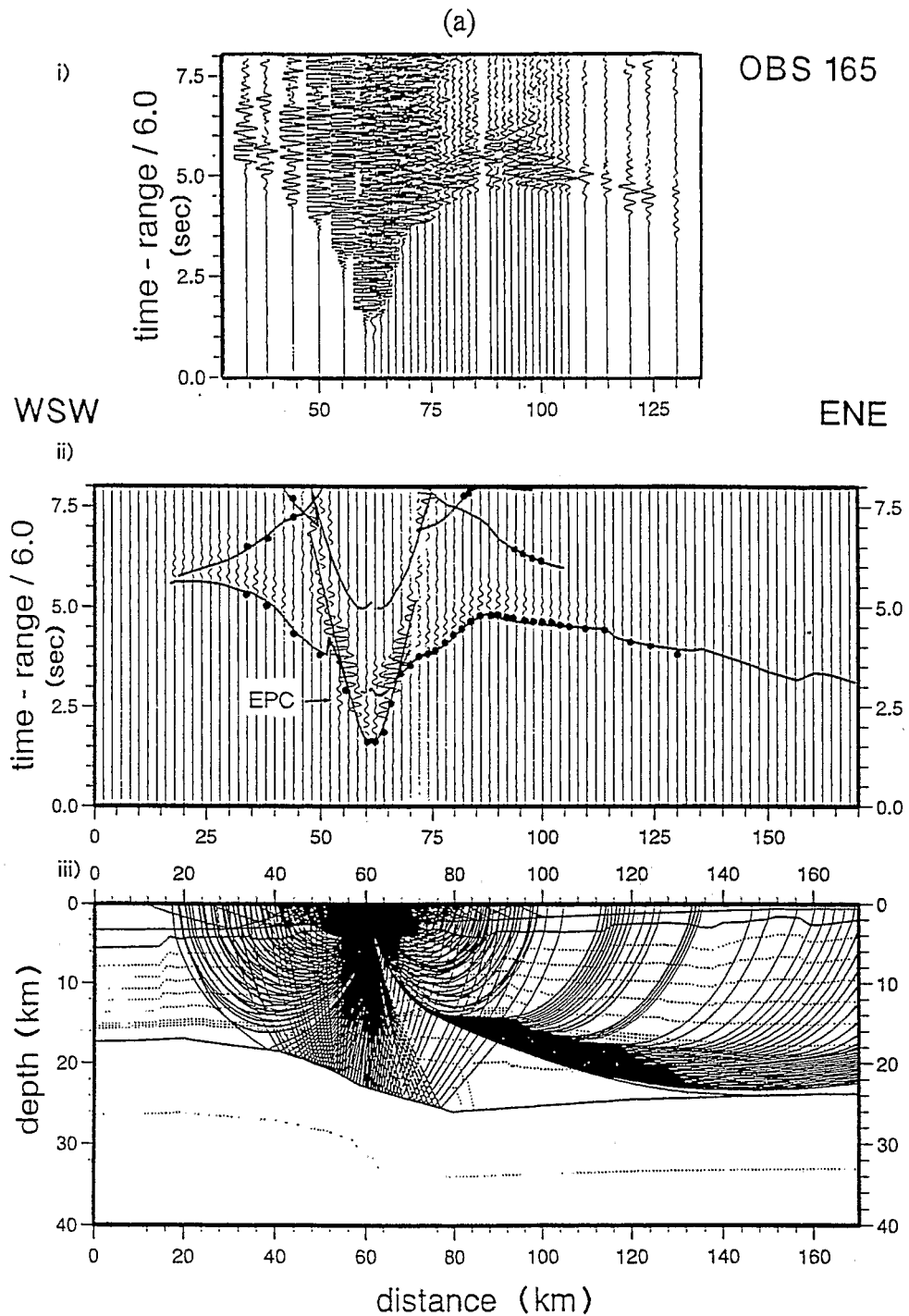
Figure 2. (a) Ray tracing of the Côte d'Ivoire–Ghana margin final model for OBS 165. (i) Observed seismograms recorded by the vertical-component geophone. The section has been plotted with west to the left and reduced at 6 km s^{-1}. The data have also been range corrected and charge-weight balanced for modelling. (ii) Synthetic seismograms are plotted with a reduction velocity of 6 km s^{-1}. End-point contributions are marked EPC—see Thomson & Chapman (1986). Observed traveltime picks for the explosive shots are indicated by dots, and the geometrical ray-traced solution by a solid line. Dot size gives an indication of the modelling misfit. (iii) Ray diagram showing general ray coverage. (b) As (a) for OBS 215. (c) Ray tracing of the Côte d'Ivoire–Ghana margin final model for OBS 3. (i) Observed seismograms recorded by a hydrophone. The section has been plotted with west to the left and reduced at 6 km s^{-1}. The data have been range-corrected for modelling. (ii) Synthetic seismograms are plotted with a reduction velocity of 6 km s^{-1}. Observed traveltime picks for the airgun shots are indicated by dots and the geometrical ray-traced solution by a solid line. Dot size gives an indication of the modelling misfit. (iii) Ray diagram showing general ray coverage. (d) As (c) for OBS 5.
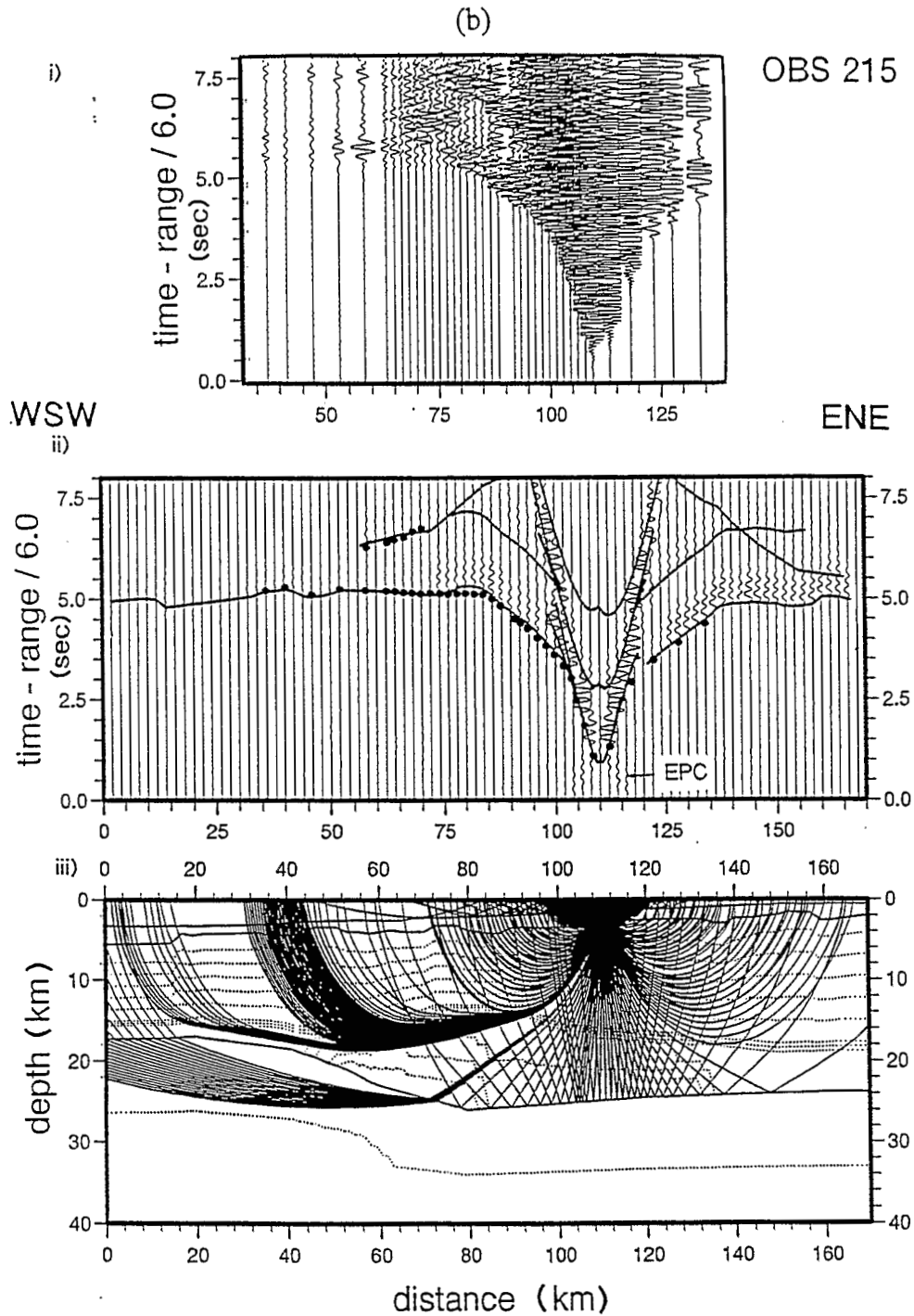
Figure 2. (*Continued.*)

Again data quality is generally high with good signal coherence between traces and a good correlation of phases. Inspection of this data reveals that the airgun source array provided a characteristic, repeatable and predictable signature, simplifying identification of later arriving phases and processing. Particular features of these sections are as follows.

(1) First arrivals can be observed to ranges of up to 90 km from receivers, with arrivals generally identified as Pg or Pn phases.

(2) Ps and PsP phases are observed at close-offset, and are mostly obscured by large-amplitude water waves. These phases are used to constrain sediment layer thickness and velocity gradient better when they are clearly identifiable in the seismic data.

(3) A significant variation in Pg and Pn amplitudes is observed as a function of offset, particularly at the Moho triplication. Modelling of these amplitude variations strongly constrains lower-crust and upper-mantle velocity gradients along almost the entire line.

(4) PmP arrivals are observed, although their onset is difficult to ascertain exactly due to the length of the source
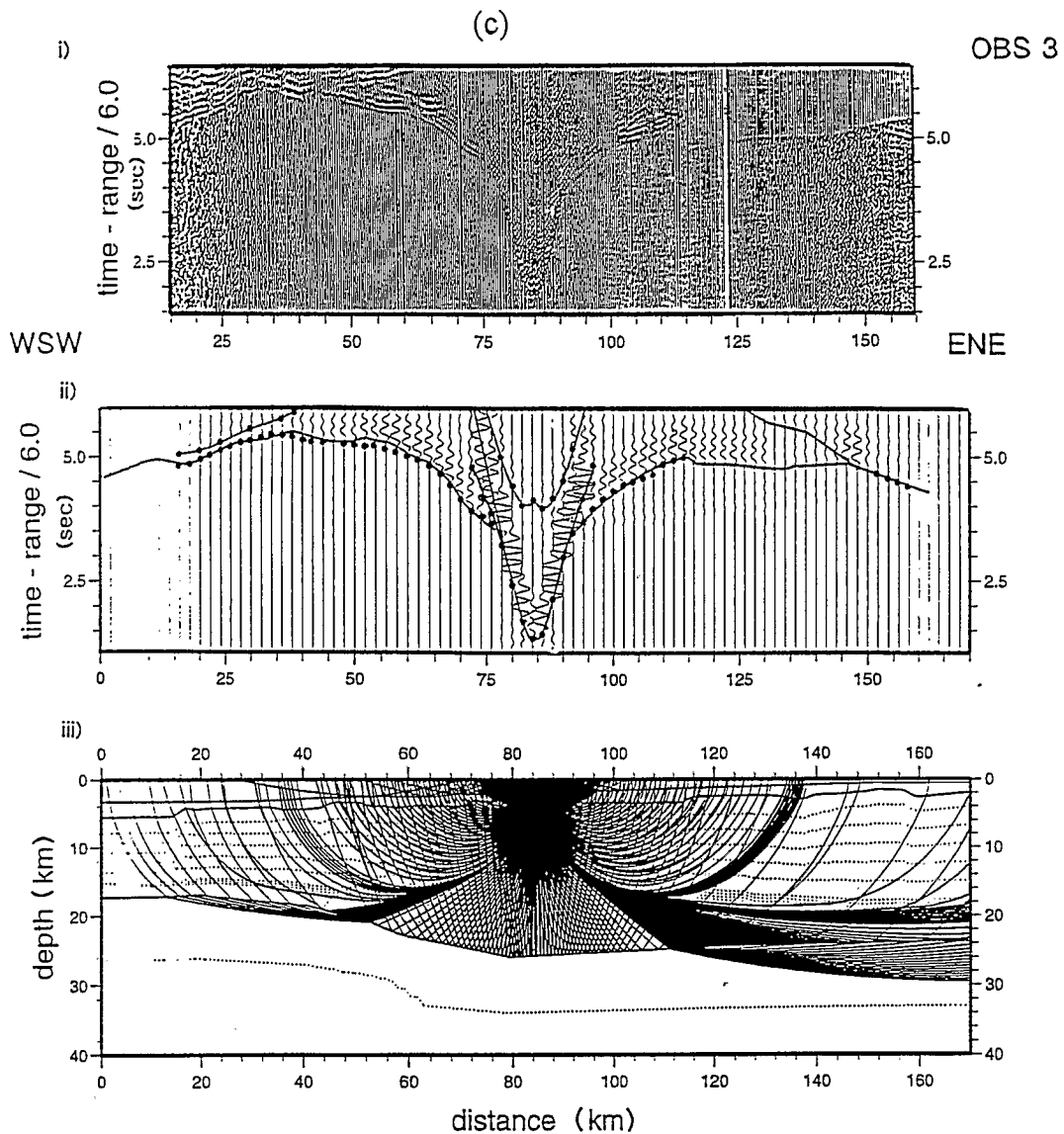
Figure 2. *(Continued.)*

wavelet and the numerous, subparallel secondary phases that arrive close behind the first arrivals. These later phases are interpreted as multiples generated within the sedimentary layer.

4 BEST-FITTING MODEL

Final ray-traced solutions for the four example OBS data sections are shown in Figs 2(a)–(d). The final best-fitting model is shown in Fig. 3, together with velocity–depth profiles (at annotated locations along the model) that best demonstrate the variation in crustal structure with offset.

The structure of the deep Ivorian Basin is highly 2-D in cross-section, with sea-floor topography varying by more than 2000 m. The final model is defined by four blocks with up to 65 points of varying separation per interface. At each point the P- and S-wave velocities, depth, offset and density are specified. The main features of the final model are as follows.

(1) The sedimentary sequence is adequately modelled by a single layer with velocities in the range 1.8 to 2.5 km s^{-1}. These

sediments are rather uniform in thickness, but reach a maximum of approximately 3.1 km thick at the westerly end of the line beneath OBS 055. A single layer was used primarily because very few Ps arrivals are observed as first arrivals at close offset, and only PsP reflections are observed for shots up to ~5 km on either side of the instrument location.

(2) The upper surface of the acoustic basement is modelled with a velocity of 3.2–3.6 km s^{-1}. This surface undulates, to match the variations observed in the first-arrival traveltime curves, and is consistent with the reflection data, which shows the top of the acoustic basement surface as a series of rotated blocks and accompanying half-grabens (Fig. 4).

(3) The lowermost crust is modelled with an average velocity of ~6.8 km s^{-1}. In the central area, a high-velocity zone, reaching a maximum of 7.2–7.4 km s^{-1} at the base of the crust, is modelled to fit the arrival times and amplitudes of lower-crustal phases. This higher-velocity region coincides with the area of most rapid crustal thinning.

(4) No first-order discontinuities within the crust were required to model the observed data. However, changes in
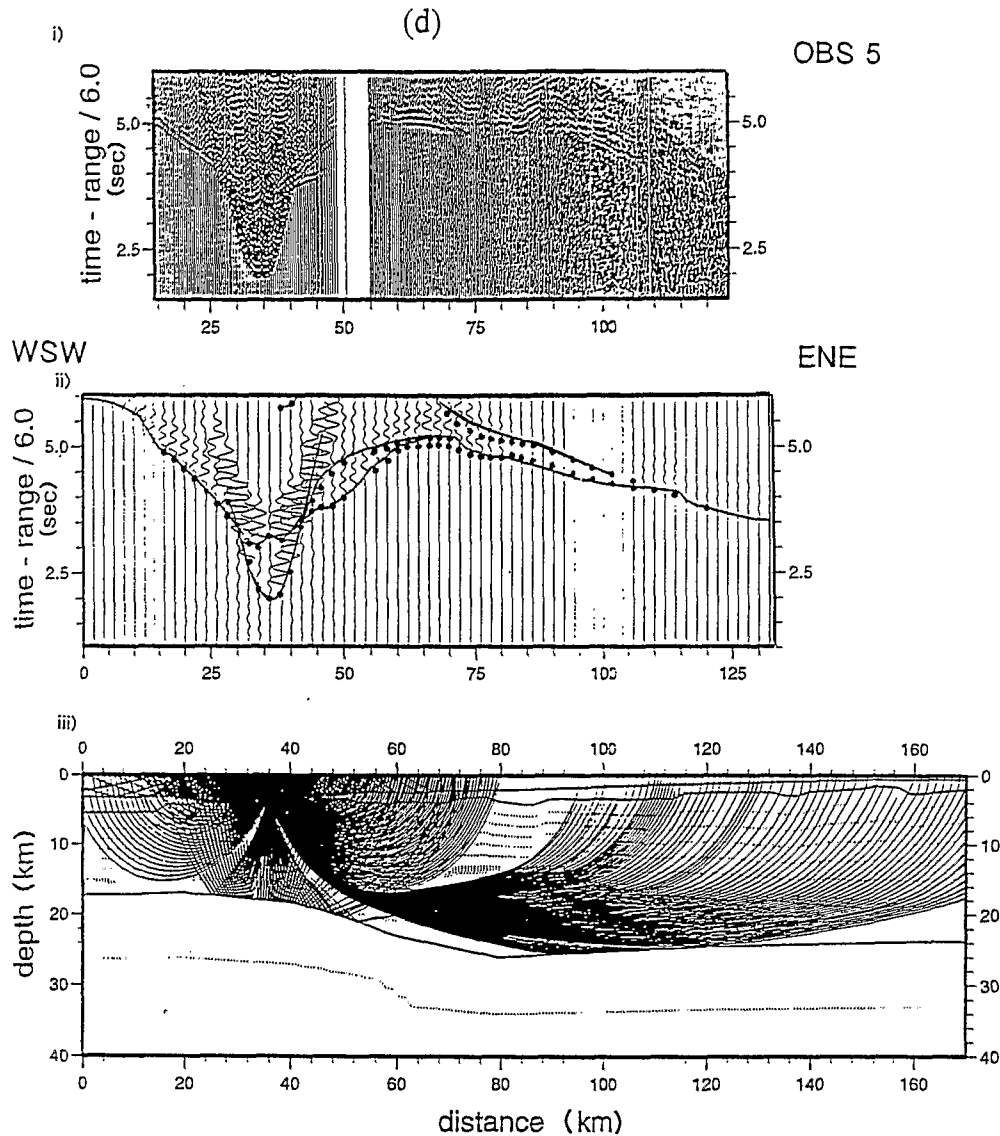
Figure 2. *(Continued.)*

velocity gradient with depth, incorporated using a second-order discontinuity, were necessary to fit the traveltimes of lower-crustal diving rays. An average gradient of ~0.2 s^{-1} in the upper crust and ~0.05 s^{-1} in the lower were required to match observed arrivals. The change in gradient occurs at ~16–18 km below sea level—corresponding approximately to the 6.5 km s^{-1} velocity contour.

(5) The crust thins rapidly over a distance of ~30 km beneath the centre of the line, from an average Moho depth of 24 km below sea level at the eastern end of the model to ~17 km at the western end. The depth to, and geometry of, the Moho are controlled mainly by the apparent truncation of observed crustal arrivals and the onset of the *Pn* phase when observed. About 150 km of the Moho are constrained in this way (see Fig. 3).

(6) The upper mantle is modelled with an average velocity of ~8.0 km s^{-1} and gradient of ~0.02 s^{-1}.

(7) Moho reflections have been ray traced for each OBS, although they are not necessarily observed extensively on all record sections. The calculated *PmP* phases generally have comparable amplitudes to, and arrive close behind, the first arrivals, which makes their exact onset difficult to identify and model, and also explains the difficulty encountered in identifying observed *PmP* phases at all in some locations.

As previously described, the final model produces synthetic seismograms that show a good overall traveltime fit with the observed data. The variations in amplitude with range have also been satisfactorily modelled. The crustal velocity structure, including both the sediments and acoustic basement, is well constrained by many crossing ray paths generated by forward- and reverse-direction profiles from adjacent instrument positions. The lack of observed *Pn* arrivals results in the velocity structure of the upper mantle not being well constrained, although the *Pn* arrivals that are observed have been well matched. Ray tracing of these arrivals provides the uppermost mantle velocity, the velocity contrast across the Moho, and its depth and geometry along most of the model length (see Fig. 3). The variation of upper-mantle velocity with depth is not readily resolvable from this data set.
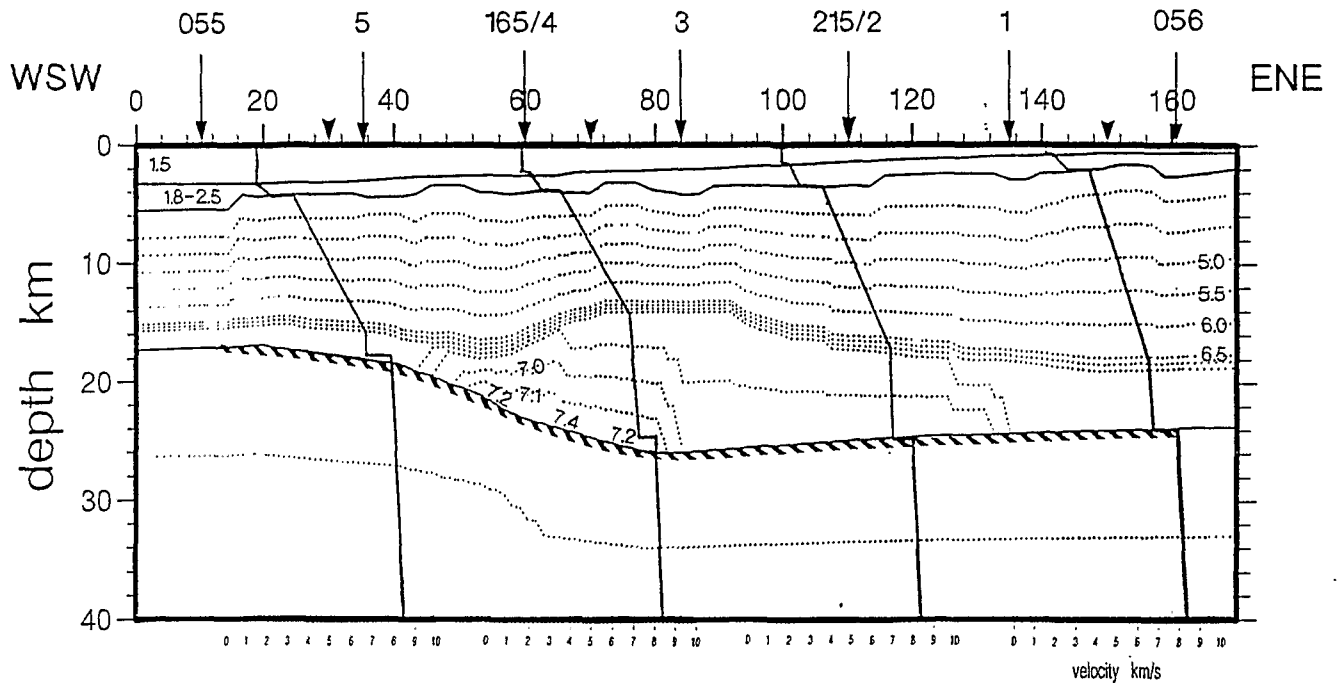
Figure 3. Final velocity–depth model. OBS locations are indicated by numbered arrows. Dotted lines show velocity contours in km s^{-1}. Velocity–depth profiles at intervals along the model (located by arrow heads) are also shown for reference. Diagonal stripes indicate the length of the Moho constrained by the ray tracing.
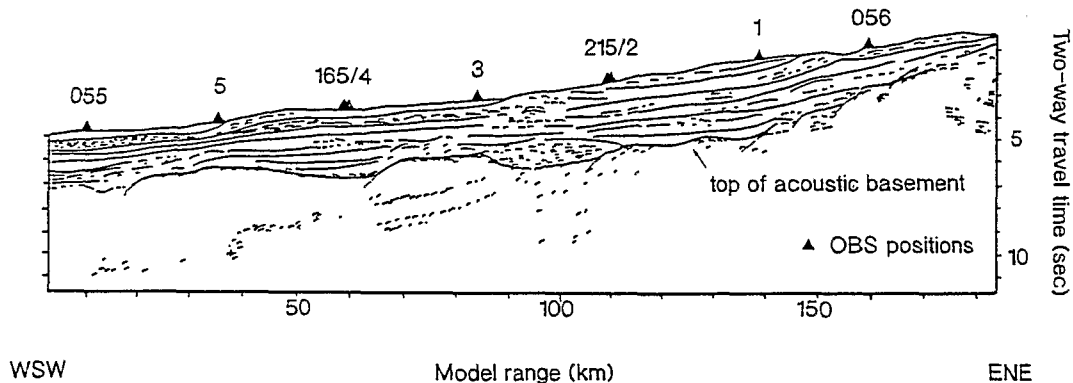

Figure 4. Line drawing of the 24-fold normal-incidence seismic reflection data collected along the wide-angle refraction line. Note the undulating acoustic basement surface.

5 GRAVITY MODELLING

The best-fitting seismic model was tested by modelling the coincident free-air gravity anomaly obtained from both the Haxby 5′ gridded gravity field of the world's oceans (Haxby 1987—see Fig. 5) and underway shipboard measurements along the CD55 seismic line. Fig. 5 clearly shows the trend of the Romanche Fracture Zone and the Guinea Basin. The intersection of the Romanche Fracture Zone with the Côte d'Ivoire–Ghana Ridge can also be observed, together with its extension running co-linear eastwards along the Ghana margin from 1°W (see Fig. 1). The seismic line is located slightly north of the Côte d'Ivoire–Ghana Ridge, in an area where the trend of the gravity contours implies a more NW–SE orientation of the margin.

The detailed gravity anomaly shown in Fig. 6 combines the Haxby gravity values with the observed data, and has been

filtered to remove short-wavelength noise. Looking at the combined anomaly in this region in more detail (Fig. 5 insert for the long-wavelength and Fig. 6 for the combined free-air anomaly), we can see that the profile traverses approximately perpendicular to the general trend of the contours, from an ~10 mgal anomaly in the east to ~ −60 mgal more oceanwards in the west.

The best-fitting seismic model (Fig. 3) was converted to a density model using the mean velocity–density relationship of Nafe & Drake (1957) (see also Barton 1986; Ludwig *et al.* 1970; Nafe & Drake 1962), with densities in Mg m^{-3} calculated initially from the model velocities. The free-air gravity anomaly was calculated using a 2-D gravity program based on Talwani, Worzel & Landisman's (1959) algorithm. The seismic model was directly converted into a density model without changing any interface geometry, layer thickness or adding additional layers, except for the 'high' velocity region and the lower crust,
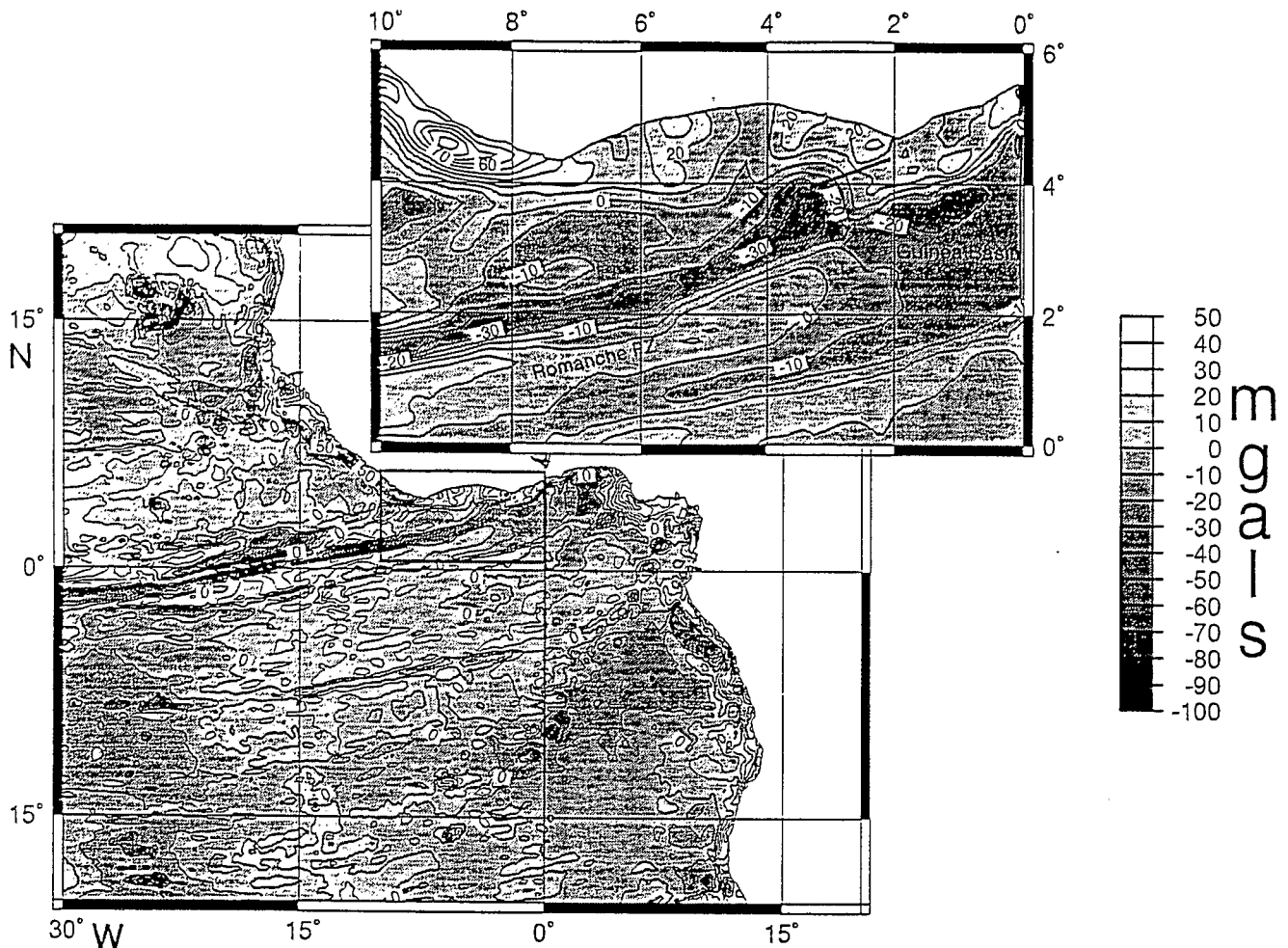
Figure 5. Free-air gravity map of the Côte d'Ivoire–Ghana margin region using data extracted from the Haxby (1987) 5' gridded data set. Contours are at 10 mgal intervals. Note how the Romanche Fracture Zone is clearly outlined—*cf.* Fig. 1. Insert: detail of the area covered by Fig. 1. The wide-angle seismic line location is also shown for reference as a solid line.

which were defined by separate blocks rather than by second-order interfaces (seismic case), to accommodate the increase in velocity with depth, the relatively high-density block at the base of the crust and the restrictions of the gravity modelling process. Only the densities of each layer were adjusted slightly until the calculated anomaly matched the general trend of the observed along the seismic line to within ~ 3–5 mgal, which represents the error bounds on the observed data points.

The final gravity model shown in Fig. 6 is as follows.

(1) The water column and sediment layers were modelled using densities and interface geometries identical to those of the seismic model. The water column was modelled with a density of 1.03 $Mg\,m^{-3}$, while the sediments were modelled with a density of 1.89 $Mg\,m^{-3}$.

(2) The crust was divided into two layers for modelling based on the depth of the 5.5–6.0 $km\,s^{-1}$ velocity contours. The upper crust was modelled using a density of 2.60 $Mg\,m^{-3}$, and the lower crust using a density of 2.8 $Mg\,m^{-3}$.

(3) The upper mantle was modelled with a density of 3.30 $Mg\,m^{-3}$, which correlates well with the 'normal' upper-mantle densities and the velocities of the seismic model.

(4) The main feature of the gravity model is the higher-

density block (3.00 $Mg\,m^{-3}$). This block corresponds to the area of high velocity in the central region.

(5) It was not necessary to adjust the position of any interface to produce a reasonable fit.

Modelling of the gravity field has shown that the observed free-air anomaly is dominated by the effects of crustal thickness and the localized higher-density region at the base of the crust. As a check on the validity of the high-velocity/density region, the gravity anomaly was remodelled without the higher-density block. Fig. 6 shows that the anomaly calculated with this model does not fit the observed data, with an ~ 55 mgal negative misfit in the region where crustal thinning occurs. The requirement for a 'higher density' block in the base of the crust to fit the observed gravity data gives us confidence that the best-fitting seismic model is a valid solution of the seismic data.

6   DISCUSSION

Ray-trace modelling has shown that the crust thins moving oceanwards from a maximum thickness of 23.5 km to a minimum thickness of about 10–11 km beneath the upper part of
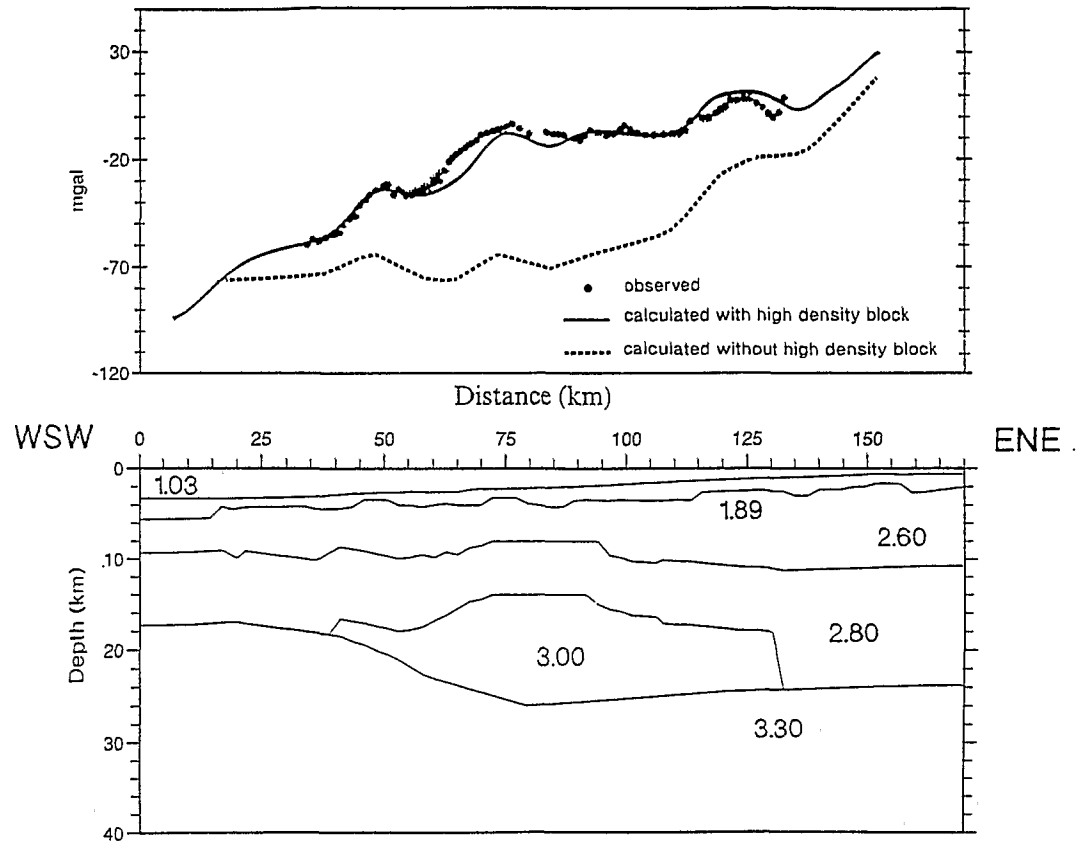
Figure 6. Calculated (solid line) and observed (dots) free-air gravity profiles along the wide-angle refraction line. Densities are in Mg m^{-3}. Interface geometries and depths are identical to the seismic model. Compare with the final seismic model shown in Fig. 3. The dashed line shows the anomaly calculated without a higher-density block in the base of the crust. Note the mismatch between the calculated and observed anomalies in the central region for the model without the high-density block.

the continental slope, continuing with an approximately constant thickness of 12–14 km to the extreme western end of the profile. Velocity–depth profiles taken from the ray-trace model (Fig. 7) also reveal a generally smooth increase in velocity with depth and an accompanying decrease in gradient. In Fig. 7, our results are compared with numerous other profiles from a wide variety of types of continental crust, including both volcanic and non-volcanic examples (White *et al.* 1987; Whitmarsh, Avedik & Saunders 1986; Ginzburg *et al.* 1985; Avedik *et al.* 1982, Powell & Sinha 1978; Hughes, White & Jones 1986; Horsefield *et al.* 1994) and oceanic crust (Spudich & Orcutt 1980). This comparison reveals that the crust beneath this part of the deep Ivorian Basin margin is continental in origin but thinned, and is similar to that found beneath typical volcanic continental margins.

Interpretation of the final seismic model (Fig. 3) indicates that normal oceanic crust was not traversed at the extreme western end of the seismic line, which appears to be located proximal to the ocean–continent transition, although ray coverage of this part of the model is not as complete as that for the remainder of the line. The crust is about 10–11 km thick at the western end of the line as compared with the average normal oceanic crustal thickness of ~7.1±0.8 km (White *et al.* 1992), and has velocities more typical of those of thinned continental crust. At the western end of the study area only minor variations in crustal thickness and velocity as a function of offset are observed, in contrast to the region underlain by normal continental crust, which exhibits highly

variable relief on the upper acoustic basement surface. Such variable relief is also observed on the normal incidence seismic reflection section and can be interpreted as a series of extensional tilted blocks and half-grabens that parallel the geometry of the margin, and continue oceanwards until the foot of the continental slope. The lower crust and Moho appear far more uniform. Wide-angle seismic modelling constrains the Moho depth to ~23–25 km below sea level beneath the shelf edge, shoaling rapidly to ~16–17 km at the foot of the continental slope—a dip of some 13°. This fairly gentle thinning is reflected in the seabed topography and is similar to that found beneath rifted (~10° at the Goban Spur, Horsefield *et al.* 1994) rather than transform margins (~43° further east on the Ghana margin, Edwards *et al.* 1996). This similarity is also supported by the uniform thickness and geometry of the sediment layer, which is comparable to that observed at typical rifted margins (*cf.* the Biscay and Goban Spur margins—Whitmarsh *et al.* 1986; Horsefield *et al.* 1994) as opposed to the larger sediment wedges typical of other transform margins (Todd *et al.* 1988; Lorenzo *et al.* 1991).

From the velocity model, a region of higher velocity is observed in the centre of the line, with velocities in the range 6.8–7.4 km s^{-1}, and this is overlain by a thinned continental crust. Gravity modelling also requires a region of higher density to match the observed free-air anomaly. These velocities and densities imply one of the following:

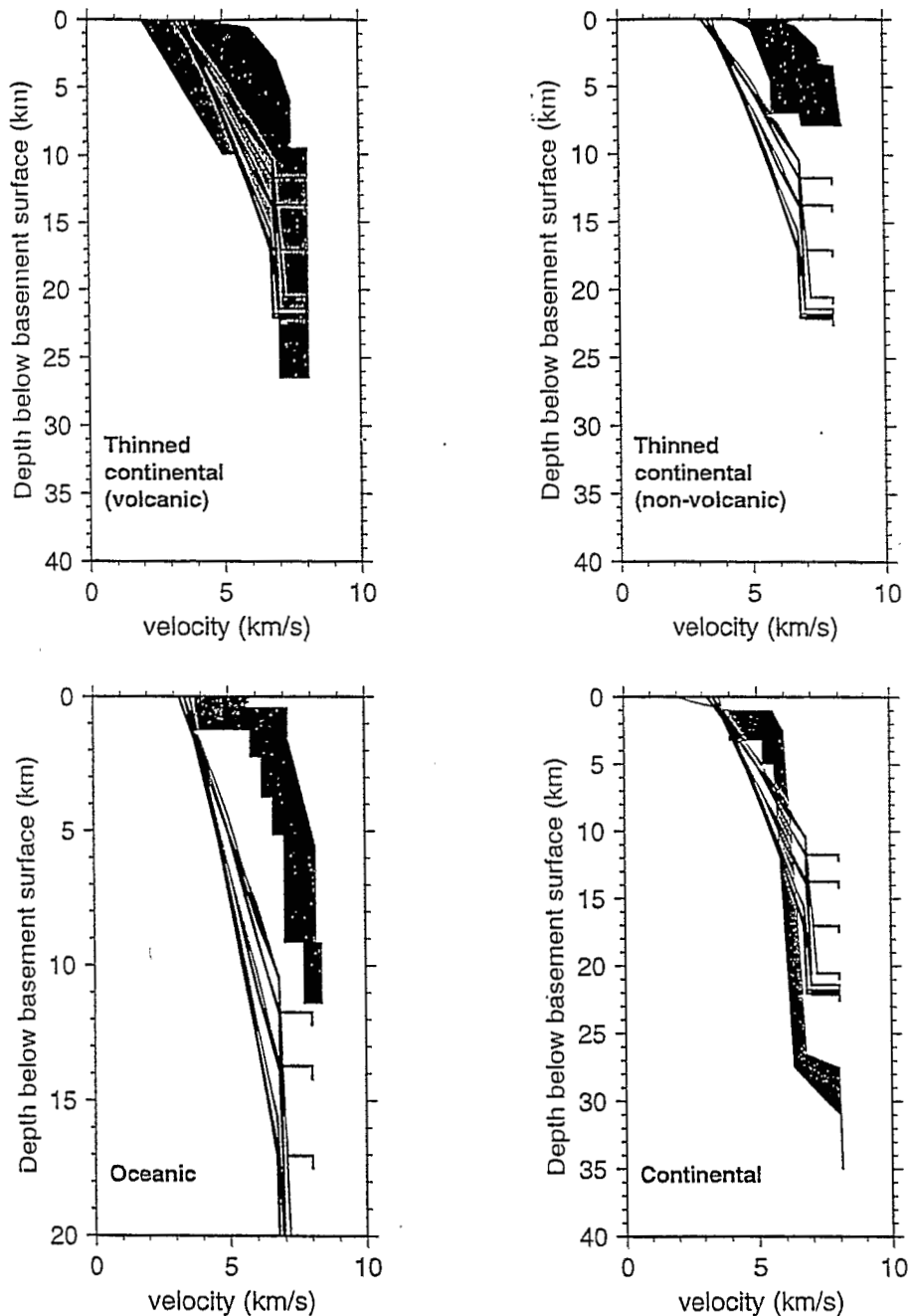(1) the continental crust was already quite heterogeneous

Figure 7. Comparison of velocity–depth profiles taken from the best-fitting seismic model, with envelopes (shaded) of normal oceanic, continental, and volcanic and non-volcanic continental-margin profiles. See text for references, in addition to Hinz, Dastmann & Fitsch (1982), Morgan, Barton & White (1989), Morgan (1988), Mutter & Zehnder (1988), Mutter, Buck & Zehnder (1988) and White (1979, 1984). Note how the velocity profiles fall largely within the envelope of those observed at volcanic continental margins.

before rifting took place, i.e. the high-density and high-velocity rocks observed onshore are also present offshore and were incorporated into the crust prior to rifting (Sage 1994);

(2) the normal thinned continental crust has been altered in some way, for example by significant intrusion of basic magma into the base of the crust (cf. the Hatton Bank—White et al. 1987); or

(3) the zone is composed of serpentinized upper-mantle material, caused by shearing along the transform margin, generating crustal fracturing and enabling circulation of sea water to deep levels (Bonatti 1978; Fox & Gallo 1986; Edwards

et al. 1996). This latter explanation seems unlikely, however, and can be discounted on the basis that the transform fault itself lies approximately 50 km to the south-east.

The seismic and gravity modelling described in this paper define the shape of the high-velocity body and locate it in the base of the crust, similar to structures observed at rifted margins, and tend to support the underplating hypothesis rather than that the crust is heterogeneous prior to rifting. Similar lower-crustal features are observed at the Southern Exmouth Plateau transform margin, whose evolution appears
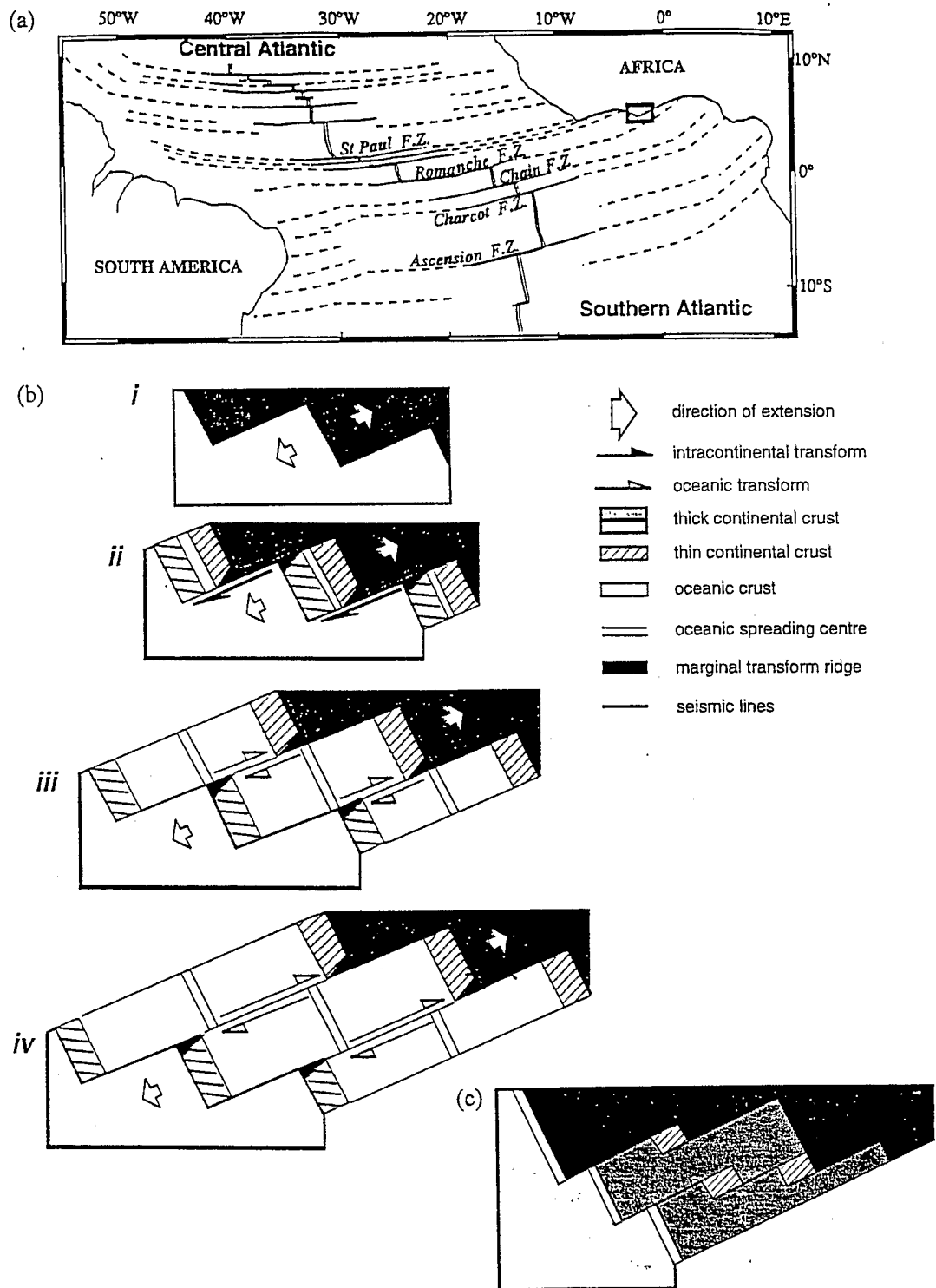
Figure 8. (a) Schematic diagram showing the equatorial Atlantic fracture zones and associated continental margins. Note how the continental margins offshore the Côte d'Ivoire and Ghana are associated with the geometry of the Romanche Fracture Zone. The boxed area indicates the region surveyed by cruises EQUAREF, EQUASIS and CD55. (b) A simplified and schematic model of margin evolution (after Mascle & Blarez 1987; Mascle *et al.* 1996). (i) Initial intracontinental transform rifting of the African and South American plates. (ii) Generation of thinned continental crust in rift segments separated by transforms. (iii) Progressive rifting with the development of oceanic crust and the juxtaposition of old continental against new oceanic lithosphere. Note the development of marginal transform ridges. (iv) Mature stage. Thermal subsidence and the juxtaposition of thinned continental crust against oceanic crust on either side of a transform fault. Locations of the seismic line presented here and another from CD55 located further east and which shows no evidence of underplating (Edwards *et al.* 1996) are shown for reference. Note how the lack of underplating of the eastern line can be explained by the fact that thick continental crust is juxtaposed against oceanic crust by the transform while the western line lies on a normally rifted continental margin. (c) An alternative mechanism for generating localized rifted continental crust in a transform environment—a series of pull-apart basins.

to have been accompanied by significant magmatic activity (Lorenzo *et al.* 1991), and along the south-western Barents Sea margin, where the high velocities and densities are attributed to the emplacement of material via mantle diapirism in a narrow pull-apart basin (Eldholm, Faledie & Myhre 1987). However, the majority of other transform margins surveyed, and other parts of the Ghana margin, show no signs of underplating (Edwards *et al.* 1996).

Mechanisms that may account for the observed underplating and cannot be discounted by the data presented here are as follows: (1) a finite rate of extension (Bown & White 1995) in localized areas along the transform margin; (2) the crustal extension observed on this part of the margin was generated in one of a series of pull-apart basins (see Fig. 8); (3) the margin did not evolve by a purely transform mechanism (Mascle *et al.* 1996); or (4) a combination of these mechanisms. These modes of formation could account for the fact that underplating is not observed along the entire length of the Côte d'Ivoire–Ghana margin and is not generally observed on all transform margin transects.

The results presented in this paper, combined with those from other parts of the margin (e.g. Mascle, Blarez & Marinho 1988; Edwards *et al.* 1996), tend to support the hypothesis that the Côte d'Ivoire–Ghana margin is not a entirely a transform margin, but that a component of rifting occurred prior to, or contemporaneously with, dominant transform motion (Blarez *et al.* 1987). Our results are consistent with the model presented by Mascle *et al.* (1996) (Fig. 8), in which the Côte d'Ivoire–Ghana margin was created as a series of rifted and transform segments, defined now by the geometry of the equatorial coastline of West Africa and its accompanying offshore bathymetry (see Fig. 1). The favoured model of margin formation is as follows. Initially two continental plates are rifted apart, perhaps along pre-existing lines of weakness, about a pole of rotation located towards the north (see Fig. 8). As rifting proceeds, individual segments are separated by shear zones that accommodate the lateral motion of the two continental plates as they separate. Crustal thinning (as demonstrated by this work) occurs in the pure-rift areas, and is accompanied by sedimentation. At this stage, shear zones separate thick unstretched and thinned continental crust. Eventually, sufficient crustal thinning occurs and oceanic crust (Fig. 8) is generated at mid-ocean ridge axes located in the centre of each basin. As motion continues along each transform, eventually new, hot oceanic crust is juxtaposed against old, cold continental crust, generating a change in thermal conditions and possibly reducing the normal rate of subsidence.

ACKNOWLEDGMENTS

REFERENCES

Avedik, F., Camus, A.L., Ginzberg, A., Montadert, L., Roberts, D.G. & Whitmarsh, R.B., 1982, A seismic refraction and reflexion study of the continent–ocean transition beneath the north Biscay Margin, *Phil. Trans. R. Soc. Lond.* A, 305, 5–25.

Barton, P.J., 1986. The relationship between seismic velocity and density in the continental crust—a useful constraint?, *Geophys. J. R. astr. Soc.,* 87, 195–208.

Basile, C., Brun, J.-P. & Mascle, J., 1992. Structure et formation de la marge transformante de Cote d'Ivoire–Ghana: apports de la sismique reflexion et de la modelisation analogique, *Bull. Soc. Geol. France,* 163, 207–216.

Basile, C., Mascle, J., Popoff, M., Boullin, J.P. & Mascle, G., 1993. The Ivory Coast–Ghana transform margin: a marginal ridge structure deduced from seismic data, *Tectonophysics,* 222, 1–19.

Blarez, E., Mascle, J., Affaton, P., Robert, C., Herbin, J.-P. & Mascle, G., 1987. Géologie de la pente continentale ivoire-ghanéenne: résultats de dragages de la campagne Equamarge, *Bull. Soc. géol. France,* 8, 877–885.

Bonatti, E., 1978. Vertical tectonism in oceanic fracture zones, *Earth planet. Sci. Lett.,* 37, 369–379.

Bown, J.W. & White, R.S., 1995. The effect of finite extension rate on melt generation at continental rifts, *J. geophys, Res.,* 100, 18 011–18 029.

Chapman, C.H. & Drummond, R., 1982. Body wave seismograms in inhomogenious media using Maslov asymptotic ray theory, *Bull. seism. Soc. Am.,* 72, S277-S317.

Dehlinger, P., Couch, R.W., McManus, D.A. & Gemperle, M., 1970. Northeast Pacific structure, in *The Sea,* Vol. 4, pt. 2, p. 133, ed. Maxwell, A.E. Wiley, New York, NY.

Delteil, J.R., Valery, P., Monatdert, L., Fondeur, C., Patriat, P. & Mascle, J., 1974. Continental margin in the northern part of the Gulf of Guinee, in *The Geology of Continental Margins,* pp. 297–331, eds Burk C.A & Drake, C.L. Springer-Verlag, New York, NY.

Edwards, R.A., Whitmarsh, R.B. & Scrutton, R.A., 1996. Geophysical features and geological development of the Ghana transform continental margin, *Geomarine Lett.,* in press.

Eldholm, O., Faleide, J.I. & Myhre, A.M., 1987. Continent–ocean transition at the Western Barents Sea/Svalbard continental margin, *Geology,* 15, 1118–1122.

Fail, J.P, Montadert, L., Delteil, J.R., Valery, P. & Schlich, R., 1970. Prolongation des zones de fracture de l'Ocean Atlantique dans le Golfe de Guinee, *Earth planet. Sci. Lett.,* 7, 413–419.

Fox, P.J. & Gallo, D.G., 1986. A tectonic model for ridge-transform-ridge plate boundaries: implications for the structure of the oceanic lithosphere, *Tectonophysics,* 104, 205–242.

Ginzburg, A., Whitmarsh, R.B., Roberts, D.G., Montadert, L., Camus, A. & Avedik, F., 1985. The deep seismic structure of the northern continental margin of the Bay of Biscay, *Ann. Geophys.,* 3, 499–510.

Hamilton, E.L., 1978. Sound velocity–density relations in sea-floor sediments and rocks, *J. acoust. Soc. Am.,* 63, 366–377.

Haxby, W.F., 1987. *Gravity field of the world's oceans,* NOAA.

Hinz, K., Dostmann, H. & Fitsch, J., 1982. The continental margin of Morocco: seismic sequences, structural elements and geological development, in *Geology of the Northwest Africa Continental Margin,* pp. 34–60, eds Von Rad, U., Hinz, K., Santhein, M. & Seibold, E., Springer-Verlag, New York, NY.

Horsefield, S.J., Whitmarsh, R.B., White, R.S. & Sibuet, J.-C., 1994.

Crustal structure of the Goban Spur rifted continental margin, N.E. Atlantic, *Geophys. J. Int.,* 119, 1–19.

Hughes, V.J., White, R.S. & Jones, E.J.W., 1984. Seismic velocity structure of the northwest Scottish continental margin: some constraints imposed by amplitude studies, *Ann. Geophys.,* 2, 669–678.

LASE Study Group, 1986. Deep structure of the U.S. East Coast passive margin from large aperture seismic experiments (LASE), *Mar. Pet. Geol.,* 3, 234–242.

Le Pichon, X. & Hayes, D.E., 1971. Marginal offset fracture zones and the early opening of the South Atlantic, *J. geophys, Res.,* 76, 6283–6293.

Lorenzo, J.M., Mutter, J.C., Larson, R.C. & the NASE study group, 1991. Development of the continent–ocean transform boundary at the Southern Exmouth Plateau, *Geology,* 19, 843–846.

Ludwig, J.W., Nafe, J.E. & Drake, C.L., 1970. Seismic refraction, in *The Sea,* Vol 4, pp. 53–84, ed. Maxwell, A.E. Wiley, New York, NY.

Mascle, J. & Blarez, E., 1987. Evidence for transform margin evolution from the Cote d'Ivoire–Ghana continental margin, *Nature,* 326, 378–381.

Mascle, J., Blarez, E. & Marinho, M., 1988. The shallow structures of the Guinea and Ivory Coast–Ghana transform margins: their bearing on the equatorial Atlantic Mesozoic evolution, *Tectonophysics,* 155, 193–209.

Mascle, J., Lohmann, P., Clift, P. & the ODP 159 Scientific Party, 1996. Development of a passive transform margin: Côte d'Ivoire–Ghana Transform margin; ODP leg 159 preliminary results, *Geomarine Lett,* submitted.

Morgan, J.V, 1988. Seismic studies over continental margins, *PhD thesis,* University of Cambridge, UK.

Morgan, J.V., Barton, P.J. & White, R.S., 1989. The Hatton Bank continental margin—III. Structure from wide-angle OBS and multichannel seismic refraction profiles, *Geophys. J. Int.,* 98, 367–384.

Mutter, J.C. & Zehnder, C.M., 1988. Deep crustal magmatic processes: The inception of seafloor spreading in the Norwegian–Greenland Sea, in *Early Tertiary Volcanism and the Opening of the North Atlantic,* Spec. Publ. Geol. Soc. Lond., 39, 34–48.

Mutter, J.C., Buck, W.R. & Zehnder, C.M., 1988. Convective partial melting I—a model for the formation of thick basaltic sequences during the initiation of spreading, *J. geophys. Res.,* 93, 1031–1048.

Nafe, J.E. & Drake, C.L., 1957. Variation with depth in shallow and deep water marine sediments of porosity, density and the velocities of compressional and shear waves, *Geophysics,* 22, 523–552.

Nafe, J.E. & Drake, C.L., 1962. Physical properties of marine sediments, in *The Sea* Vol. 3, pp. 794–815, ed. Hill, M.N. Wiley, New York, NY.

Peirce, C., 1990. Crustal structure of the Africa–Eurasia plate boundary, *PhD thesis,* University of Cambridge, UK.

Peirce, C. & Barton, P.J., 1991. Crustal structure of the Madeira–Tore Rise, eastern North Atlantic—results of a DOBS wide-angle and normal incidence seismic experiment in the Josephine Seamount region, *Geophys. J. Int.,* 106, 357–378.

Powell, C.M.R. & Sinha, M.C., 1987. The PUMA experiment west of Lewis, UK, *Geophys. J. R. astr. Soc.,* 89, 259–264.

Recq, M., 1982. Anomalies de propagation des ondes P a l'est de la Ride de Davie, *Tectonophysics,* 82, p189–206.

Sage, F., 1994. Structure crustale d'une marge transformante et du domaine oceanique adjacent: exemple de le marge de Côte d'Ivoire–Ghana, *PhD thesis,* University of Paris VI, France.

Sibuet, J.C. & Mascle, J., 1978. Plate kinematic implications of Atlantic equatorial fracture zones trends, *J. geophys. Res.,* 83, 3401–3421.

Spudich, P. & Orcutt, J., 1980. A new look at the seismic velocity structure of the oceanic crust, *Rev. Geophys.,* 18, 627–645.

Talwani, M., Worzel, J.L. & Landisman, M., 1959. Rapid gravity calculations for two-dimensional bodies with application to the Mendocino Submarine Fracture Zone, *J. Geophys, Res.,* 64, 49–59.

Thomson, C.J. & Chapman, C.H., 1986. End-point contributions to synthetic seismograms, *Geophys. J. R. astr. Soc.,* 87, 285–294.

Todd, B.J., Reid, I. & Keen, C., 1988. Crustal structure across the southwest Newfoundland transform margin, *Can. J. Earth Sci.,* 744–759.

Wessel, P. & Smith, W.H.F., 1991. *The GMT-system, technical reference and cookbook,* p. 39, Scripps Institute of Oceanography internal report.

White, R.S., 1979. Oceanic upper crustal structure from variable angle seismic reflection-refraction profiles, *Geophys. J. R. astr. Soc.,* 57, 683–726.

White, R.S., 1984. Atlantic Ocean crust: seismic structure of a slow spreading ridge, in *Ophiolites and Oceanic Lithosphere,* eds Gass, I.G., Lippard, S.J. & Shelton, A.N., Spec. Publ. Geol. Soc. Lond., 13, 34–44.

White, R.S. & McKenzie, D.P., 1989. Magmatism at rift zones: the generation of volcanic continental margins and flood basalts, *J. geophys. Res.,* 94, 7685–7729.

White, R.S., McKenzie, D.P. & O'Nions, R.K., 1992. Oceanic crustal thickness from seismic measurements at rare earth element inversions, *J. geophys. Res.,* 97, 19683–19715.

White, R.S., Spence, G.D., Fowler, S.R., McKenzie, D.P., Westbrook, G.K. & Bowen, A.N., 1987. Magmatism at rifted continental margins, *Nature,* 330, 439–444.

Whitmarsh, R.B., Avedik, F. & Saunders, M.R., 1986. The seismic structure of thinned continental crust in the northern Bay of Biscay, *Geophys. J. R. astr. Soc.,* 86, 589–602.

Wilson, J.T., 1965. A new class of faults and their bearing on continental drift, *Nature,* 207, 343–347.